PHYSICAL REVIEW B **99**, 155111 (2019)

Ultrafast quasiparticle dynamics in the correlated semimetal $Ca_3Ru_2O_7$

Yakun Yuan,[1] Peter Kissin,[2] Danilo Puggioni,[3] Kevin Cremin,[2] Shiming Lei,[1] Yu Wang,[4] Zhiqiang Mao,[4,5]
James M. Rondinelli,[3] Richard D. Averitt,[2,*] and Venkatraman Gopalan[1,5,†]
[1]*Materials Research Institute and Department of Materials Science & Engineering, Pennsylvania State University, University Park, Pennsylvania 16802, USA*
[2]*Department of Physics, University of California San Diego, La Jolla, California 92093, USA*
[3]*Department of Materials Science & Engineering, Northwestern University, Evanston, Illinois 60208, USA*
[4]*Department of Physics & Engineering Physics, Tulane University, New Orleans, Louisiana 70118, USA*
[5]*Department of Physics, Pennsylvania State University, University Park, Pennsylvania 16802, USA*

(Received 7 September 2018; revised manuscript received 13 March 2019; published 4 April 2019)

The correlated polar semimetal $Ca_3Ru_2O_7$ exhibits a rich phase diagram including two magnetic transitions ($T_N = 56$ K and $T_C = 48$ K) with the appearance of an insulating-like pseudogap (at T_C). In addition, there is a crossover back to metallic behavior at $T^* = 30$ K, the origin of which is still under debate. We utilized ultrafast optical-pump optical-probe spectroscopy to investigate quasiparticle dynamics as a function of temperature in this enigmatic quantum material. We identify two dynamical processes, both of which are influenced by the onset of the pseudogap. This includes electron-phonon relaxation and, below T_C, the onset of a phonon bottleneck hindering the relaxation of quasiparticles across the pseudogap. We introduce a gap-modified two-temperature model to describe the temperature dependence of electron-phonon thermalization, and use the Rothwarf-Taylor to model the phonon bottleneck. In conjunction with density functional theory, our experimental results synergistically reveal the origin of the T-dependent pseudogap. Further, our data and analysis indicate that T^* emerges as a natural consequence of T-dependent gapping out of carriers, and does not correspond to a separate electronic transition. Our results highlight the value of low-fluence ultrafast optics as a sensitive probe of low-energy electronic structure, thermodynamic parameters, and transport properties of Ruddlesden-Popper ruthenates.

DOI: 10.1103/PhysRevB.99.155111

I. INTRODUCTION

Ruddlesden-Popper ruthenates have received tremendous research interest since the discovery of superconductivity in Sr_2RuO_4, which is the only non-copper-based superconductor isostructural to $La_{2-x}(Sr, Ba)_xCuO_4$ [1,2]. Previous studies on $Ca_3Ru_2O_7$ [space group $Bb2_1m$, Fig. 1(a)] have revealed a rich interplay between spin, lattice, and electronic degrees of freedom [3–8]. As shown in Fig. 1(b), between $T_C = 48$ K and $T_N = 56$ K, the spins in $Ca_3Ru_2O_7$ align ferromagnetically within the *a*-*b* plane and antiferromagnetically (AFM) along the *c* axis, with the spins oriented along the *a* axis (AFM-*a*). At $T_C = 48$ K, the resistivity begins to display insulating behavior and the spins align along the *b* axis (AFM-*b*) [6], with metallic resistivity reemerging below $T^* = 30$ K [4,5,7].

The electronic structure changes of $Ca_3Ru_2O_7$ at T_C and T^* require further clarification. T_C was previously thought to correspond to a Mott-type transition [5,9], however, the observation of a partial gap opening near E_F points to a Fermi surface (FS) instability [10], which suggests the appearance of a density wave [4,11], despite the unusual redistribution of optical spectral weight. While a density wave has not been directly observed in $Ca_3Ru_2O_7$, this scenario may offer new opportunities to study the emergence of charge and spin density waves in the isostructural bilayer cuprates [see Fig. 1(a)]. Recently, a Lifshitz transition was proposed as the origin of the resistivity crossover at T^* [12].

The interactions between strongly correlated degrees of freedom are often more easily disentangled when studied on their natural timescales, motivating dynamical studies of $Ca_3Ru_2O_7$ in the time domain. Optical-pump optical-probe (OPOP) spectroscopy has been used to study the relaxation dynamics of photoexcited quasiparticles (QPs) in a variety of materials [13–19]. The versatility of this technique derives from its extreme sensitivity to the formation of small gaps in the electronic density of states (DOS) near the Fermi energy E_F. The presence of a gap can be inferred from the temperature and pump fluence dependence of the QP relaxation dynamics, and may result in an increase of the relaxation time by several orders of magnitude. OPOP complements conventional frequency domain techniques in characterizing the low-energy electronic structure of quantum materials.

In this study, we investigate quasiparticle dynamics in $Ca_3Ru_2O_7$ using OPOP spectroscopy. Our data reveal the development of a pseudogap that dramatically alters the relaxation dynamics, slowing down the electron-phonon relaxation near the Fermi surface, giving rise to a relaxation component related to a phonon bottleneck associated with above-gap QP excitations. The coexistence of both relaxation channels with comparable strength in one material is unexpectedly rare,

---

[*] raveritt@ucsd.edu

[†] vxg8@psu.edu

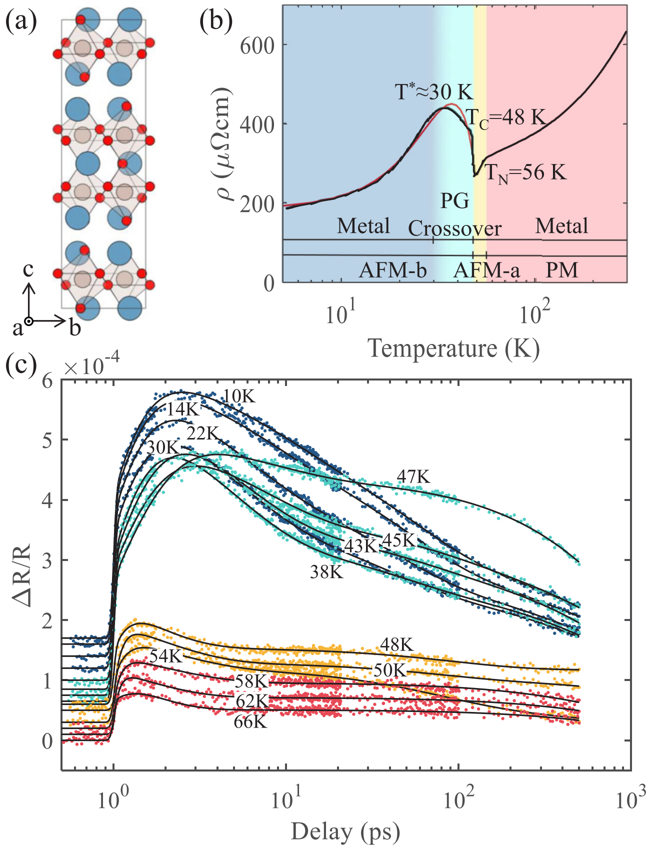

FIG. 1. (a) Atomic structure of $Ca_3Ru_2O_7$ with a $Bb2_1m$ space group. Ca, Ru, and O atoms are labeled in blue, brown, and red, respectively. (b) dc resistivity of $Ca_3Ru_2O_7$ in the *a-b* plane [4]. Regions with different colors represent different behaviors emerging at low temperature. PM stands for paramagnetic phase. The red line is a fit based on T-dependent carrier concentration and scattering rate discussed later. (c) Temperature-dependent OPOP data on $Ca_3Ru_2O_7$. Four distinct relaxation processes are clearly observed at various temperatures, color-coded to match the resistivity phase diagram in (b). Black lines are fits using the multiexponential decay model described in the text.

making $Ca_3Ru_2O_7$ a unique platform to study quasiparticle dynamics affected by both the pseudogap and Fermi surface. Analysis with a T-dependent DOS shows that the crossover at T^* can be explained as a consequence of the T-dependent gap that opens at T_C, without invoking a separate electronic transition, simplifying the understanding of the phase diagram of $Ca_3Ru_2O_7$.

II. EXPERIMENTAL METHODS

A. Optical pump-probe spectroscopy

Single crystals of $Ca_3Ru_2O_7$ were grown using the floating-zone method. OPOP measurements on $Ca_3Ru_2O_7$ used 25-fs laser pulses centered at 800 nm with a repetition rate of 209 kHz. The pump fluence was fixed at 2 $\mu J/cm^2$ for all reported measurements to ensure minimal sample heating. The sample temperature change is determined to be less than 1 K under experimental temperature >20 K, which increases to 7 K at the lowest experimental temperature 10 K [see inset of Fig. 7(b) and analysis in Sec. III D]. The probe fluence was 1 $\mu J/cm^2$. Due to the low repetition rate, the system was able to fully relax back to ground state before each pump pulse. A probe fluence dependence test verified there was no probe-induced effect. The cross-polarized pump and probe beams were focused onto the sample to $1/e^2$ spot diameters of 70 and 40 μm, respectively. The data were collected from large, flat areas of samples cleaved in the *a-b* plane. A continuous-flow liquid helium optical cryostat was used for temperature control.

B. Time-domian thermoreflectance

Time-domain thermoreflectance (TDTR) measurements were carried out on aluminum-coated $Ca_3Ru_2O_7$ as a function of temperature using 100-fs laser pulses at 800 nm with a repetition rate of 80 MHz [20,21]. The pump was frequency doubled by a BiBO crystal and focused down to 20 μm of $1/e^2$ spot diameter, while probe at 800 nm had a spot size of 10 μm. The pump beam was modulated with an electro-optic modulator operating at 4.95 MHz.

C. Density functional theory calculations

Density functional theory (DFT) calculations were performed with the Perdew-Burke-Ernzerhof of exchange-correlation functional revised for solids [22,23] as implemented in the Vienna *ab initio* simulation package [24] with the projector-augmented wave method [25] to treat the core and valence electrons using the following electronic configurations 3*s*2, 3*p*6, 4*s*2 (Ca), 5*s*2, 4*d*6 (Ru), and 2*s*2, 2*p*4 (O), and a 500-eV plane-wave cutoff. Electron correlations in Ru-4*d* electrons were treated using the Hubbard-U (U_{eff} = 1.2 eV) method within the Dudarev formalism [26]. Spin-polarized calculations with noncollinear AFM-*b* and AFM-*a* spin order were imposed on the Ru atoms. A $7 \times 7 \times 5$ Monkhorst-Pack k-point mesh [27] and Gaussian smearing (20 meV width) was used for the Brillouin zone (BZ) sampling and integrations.

III. RESULTS AND DISCUSSION

A. Quasiparticle relaxation dynamics in $Ca_3Ru_2O_7$

Figure 1(c) shows the T dependence of the photoinduced change in fractional reflectivity $\Delta R/R$ as a function of time from 66 to 10 K. The data are plotted on a logarithmic x scale with time zero shifted to 1 ps for better visualization. The temporal resolution is 25 fs. Above 66 K, the dynamics is only weakly T dependent (For complete data set, see Supplemental Material, Sec. I [28].) Above T_C, the relaxation is biexponential, consisting of a large, fast component that relaxes on a subpicosecond timescale and a small, slow component that persists beyond the measurement window of 500 ps. Near T_N, between 58 and 54 K, the fast component slows down and the slow component becomes faster, marking the PM to AFM-*a* transition. At T_C, between 48 and 47 K, the maximum signal amplitude increases by a factor of 3 and the relaxation dynamics becomes triexponential, with a relaxation process emerging on an intermediate timescale of nearly 100 ps. These abrupt changes to the dynamics mark the first order transition to the partially gapped low-temperature phase [5]. Cooling from 47 to 10 K, the fast component first becomes faster then slows down, showing a minimum signal amplitude at 10 ps near T^*.

We fit the data to a multiexponential function of the form [16]

$$\frac{\Delta R}{R}(t) = f(t) \times (A_1 e^{-t/\tau_{d1}} + A_2 e^{-t/\tau_{d2}} + A_3 e^{-t/\tau_{d3}}), \qquad (1)$$

where $f(t) = r \times \{\frac{1}{2} + \frac{1}{2}\mathrm{erf}[\sqrt{2}(t - t_0)/\tau_p]\} + (1 - r) \times (1 - e^{-t - t_0/\tau_r})$. In $f(t)$, the first term containing the error function represents the cross correlation of the pump and probe pulses with a T-independent pulse duration τ_p. The second term containing τ_r represents the slow rise dynamics that onset mainly below T_C. r and $1 - r$ are weights for above two contributions, respectively. The main term, which contains three strongly T-dependent exponential decays, is the focus of our analysis. Detailed analysis shows that the fast component A_1, τ_{d1} and the component A_2, τ_{d2} emerging below T_C are associated with QP dynamics near E_F. The slow component A_3, τ_{d3} arises from the thermal dissipation of pump-induced energy.

B. Fast relaxation component

We first focus on the fast relaxation component A_1 and τ_{d1}. As shown in Fig. 2(a), the time constant of this fast component is subpicosecond at high temperatures and slows down upon approaching T_C. Within this temperature range, $Ca_3Ru_2O_7$ exhibits metallic behavior ($\frac{d\rho}{dT} > 0$) as shown by Fig. 1(b). Following photoexcitation, the fast relaxation dynamics of metals are governed by electron-phonon (e-ph) thermalization, which can be described using the two-temperature model (TTM) [16,29]. A central assumption of the TTM is electron-electron (e-e) scattering is much faster than electron-phonon (e-ph) scattering. Thus, the photoexcited electron subsystem can almost immediately be described with an elevated electronic temperature T_e. Subsequently, e-ph thermalization increases the lattice temperature (T_l), until a quasiequilibrium is reached between the two subsystems.

The e-ph thermalization time constant in the TTM is given by $\tau_{\text{e-ph}} = \frac{1}{g}\frac{C_e C_l}{C_e + C_l}$, where $g(T)$ is the e-ph coupling function, C_e and C_l are the specific heats for the electron and lattice subsystems, respectively. Typically, $C_l \gg C_e$ at high temperatures. On approaching 0 K, $C_e = \gamma T$ and $C_l = \beta T^3$, with $\gamma = 1.7\ \mathrm{mJ/mol_{Ru}\,K^2}$ and $\beta = 0.14\ \mathrm{mJ/mol_{Ru}\,K^4}$ for $Ca_3Ru_2O_7$ [7]. At the lowest temperature (10 K) of this OPOP study, $C_e = 17 \ll 140\ \mathrm{mJ/mol_{Ru}\,K} = C_l$. Thus, the e-ph thermalization time at all temperatures can be further simplified as

$$\tau_{\text{e-ph}} \approx \frac{C_e}{g}. \qquad (2)$$

We approximate $g(T)$ for $Ca_3Ru_2O_7$ using an expression valid for simple metals $g(T) = dG(T)/dT$, $G(T) = 4g_\infty(T/\theta_D)^5 \int_0^{\theta_D/T} \frac{x^4}{e^x - 1}dx$ [16]. The Debye temperature $\theta_D = 437$ K (for calculations, see Supplemental Material, Sec. II [28]), leaving the constant g_∞ as the only free parameter. The T dependence of $g(T)$ is plotted in the inset of Fig. 2(c). Assuming a T-independent C_e in this temperature range, a fit to τ_{d1} above T_C, shown in the inset of Fig. 2(a), agrees well with our data, supporting the TTM description of the dynamics above T_C.

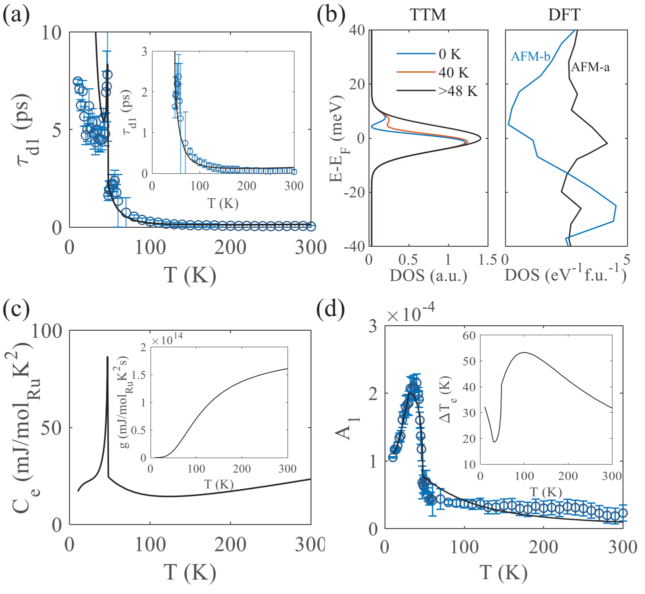

FIG. 2. (a) Temperature dependence of the electron-phonon thermalization time constant τ_{d1}. The inset shows a magnified plot on the nonzero values of τ_{d1} at high temperatures. (b) Temperature dependence of DOS near E_F obtained from TTM analysis (left panel). DOS for AFM-*a* and AFM-*b* ground states predicted by DFT (right panel). (c) Electronic heat capacity heat from TTM calculation. The inset shows the temperature-dependent electron-phonon coupling constant near the Fermi surface used for TTM analysis. (d) Amplitude of electron-phonon thermalization dynamics A_1 as a function of temperature. The fit takes values in from the DOS in (b) and the electronic specific heat yielded from (a) and shown in (c). The inset shows the electronic temperature change upon optical pump.

To account for changes in e-ph thermalization dynamics in the vicinity of T_C (e.g., both the lifetime and amplitude) we study the effect of a gap on the e-ph relaxation time by considering a phenomenological T-dependent DOS of the form

$$D_e(\epsilon) = D_0 + D_1 e^{-\frac{\epsilon^2}{w_1^2}}\left[1 - \frac{\Delta(T)}{\Delta_0} e^{-\frac{(\epsilon-\epsilon')^2}{w_2^2}}\right]. \qquad (3)$$

The summation of a constant D_0 and a Gaussian with width w_1 is often used to describe the DOS of correlated metals [16]. The term in the square brackets describes the reduction in the DOS due to the opening of a gap, with a BCS-type temperature-dependent behavior $\Delta(T) = \Delta_0 \tanh 2.2\sqrt{\frac{T_C}{T} - 1}$, where $\Delta(T)$ is the temperature-dependent gap size, and Δ_0 is the gap size at 0 K. The Gaussian centered at ϵ' with width w_2 approximates the shape of the DOS reduction due to the gap opening. The electronic specific heat can then be derived from the electronic DOS near E_F by $C_e = \frac{\partial}{\partial T}\int_{-\infty}^{\infty} \epsilon D_e(\epsilon, T) f(\epsilon, T) d\epsilon$, $\epsilon = E - E_F$, ignoring the weak temperature dependence of E_F.

Allowing the parameters of the model DOS [Eq. (3)] to vary, we fit τ_{d1} using Eq. (2) for all temperatures. The fit, plotted in Fig. 2(a), reproduces the behavior down to ∼40 K, including the slowdown as cooling down to T_C, the sudden jump at T_C, and the subsequent drop below T_C. The deviation of the fit below ∼40 K signifies the failure of the TTM at very low temperatures, which is quite general in TTM analysis because the timescale of e-e thermalization slows down and becomes comparable to the timescale of e-ph thermalization at low T [16]. The extracted DOS described by Eq. (3) and the resulting electronic specific heat C_e are plotted in Figs. 2(b) (left panel) and 2(c), respectively, with parameters of $w_1 = 6.3 \pm 0.3$ meV, $\epsilon' = 4 \pm 2$ meV, $w_2 = 4 \pm 2$ meV. In addition, we would like to point out that a gap below the Fermi level fails to fit the experimental data. The gap in DOS centered at 4 ± 2 meV qualitatively agrees with 8-meV gap observed by ARPES [10].

To further explore the emergence of the gap in the electronic density of states in the AFM-b ground state below T_C, we performed electronic structure calculations using density functional theory with static correlations (DFT+U+SOC), as shown in the right panel of Figs. 2(b) and 3. We find that the DOS in AFM-a state exhibits a peak feature near E_F, which qualitatively agrees with our single Gaussian shape of DOS above T_C. It also should be noted that the DOS extracted from the fast relaxation dynamics under TTM only captures the dynamics of electrons near E_F within the thermal activation energy scale k_BT. Thus, our measurement is not sensitive to the electronic states far away from E_F. This explains the differences between the calculations and our model DOS away from E_F. For the AFM-b ground state below T_C, band structure and DOS by DFT calculations predict a dip feature near E_F with a minimum position at ∼7 meV. This is consistent with the T-dependent DOS obtained using TTM, where a dip feature centered at 4 ± 2 meV shows up on approaching 0 K. The position of this feature yielded by DFT and TTM analysis qualitatively agrees well with each other. The computed band structures for both AFM-a and AFM-b states (shown in Fig. 3) share key features in common with established experimental results. Prominent and relatively flat bands connect M and M' near E_F, qualitatively reproducing the square Fermi surface observed in ARPES [10]. The gap primarily affects the dispersions of bands in the vicinity of M and M', resulting in Fermi surface crossings along M-M' with holelike dispersion near M and electronlike dispersion near M'. These mimic the electron and hole pockets detected by quantum oscillations at the same locations [11].

In addition, the transient amplitude A_1 can be modeled with the TTM by considering the number density of thermally activated electrons [16]:

$$A_1 \propto n_{T_e'} - n_{T_e} = \int_0^\infty D_e(\epsilon, T_e')f(\epsilon, T_e') - D_e(\epsilon, T_e)f(\epsilon, T_e)d\epsilon. \qquad (4)$$

The electronic temperature after photoexcitation T_e' is determined by $\Delta U = \int_{T_e}^{T_e'} C_e dT$, with deposited energy density ΔU. Equation (4) considers both changes in DOS and carrier population. The transient electronic temperature change ΔT_e, plotted in the inset of Fig. 2(d), is substantial, thus a transient suppression of the gap and a corresponding change in $D_e(\epsilon, T)$ at T_e and T_e' in Eq. (4) must be considered in order to reproduce the T dependence of A_1. Taking $D_e(\epsilon, T)$ from Fig. 2(b), the fit to A_1 using Eq. (4) is shown in Fig. 2(d). The excellent fit captures all characteristics over the entire temperature range of the measurement, which strongly suggests that the TTM model captures essential features of the role of the pseudogap in determining the e-ph thermalization. In addition, we also point out that the phonon bottleneck picture described later by the Rothwarf-Taylor model fails to explain these dynamics (see Supplemental Material, Sec. III [28]).

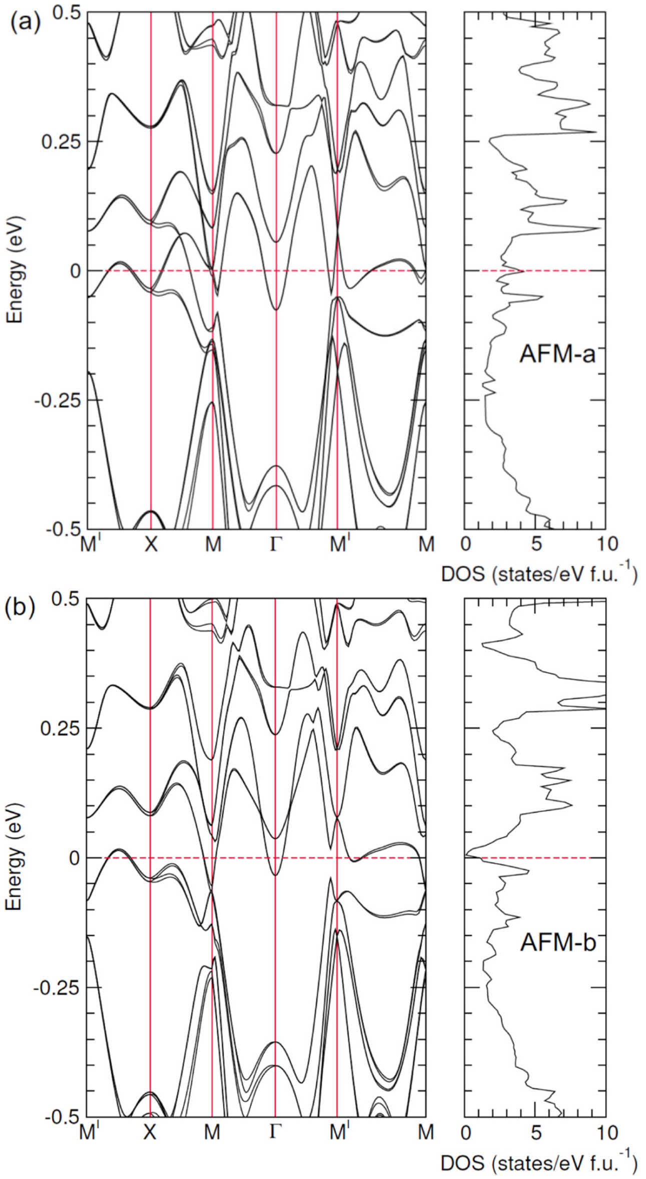

FIG. 3. (a) Band structure and DOS in AFM-a state, which is the ground state of $Ca_3Ru_2O_7$ above T_C. (b) Band structure and DOS in AFM-b state, which is the ground state of $Ca_3Ru_2O_7$ below T_C. A suppression of DOS is observed compared to AFM-a state in DOS near E_F. The minimum point of this dip locates at ∼7 meV above E_F.

The development of the gap is expected to deplete the free carriers in the system, resulting in an increase of resistivity below T_C. On the other hand, the decrease in carrier scattering

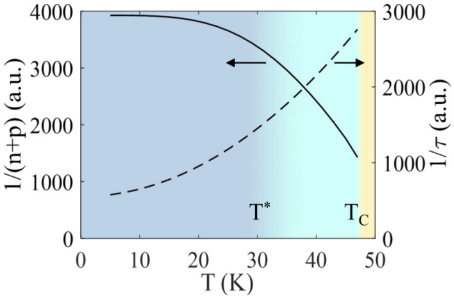

FIG. 4. $1/(n+p)$ and $1/\tau$ extracted from the pseudogap crossover region between T^* and T_C.

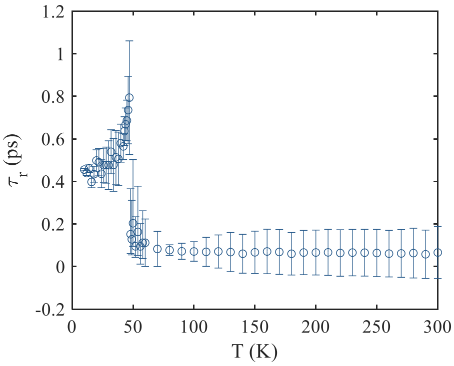

FIG. 5. T-dependent rise time τ_r in $Ca_3Ru_2O_7$. The significant increase below T_C signifies the strong phonon bottleneck regime.

rate at low temperatures will reduce the resistivity. Using the DOS employed for the TTM modeling, we investigate if the T-dependent carrier density and scattering time is responsible for the upturn in resistivity ($\frac{d\rho}{dT} < 0$) between T^* and T_C. We approximate the population of free electrons (n) and holes (p) to be $n = \int_{-\infty}^{\infty} D_e(\epsilon, T) f(\epsilon, T) d\epsilon - N_1$ and $p = \int_{-\infty}^{\infty} D_e(\epsilon, T)[1 - f(\epsilon, T)] d\epsilon - N_2$, where N_1 and N_2 are populations of localized electrons and holes near E_F. The total free carriers can be written as $n + p = \int_{-\infty}^{\infty} D_e(\epsilon, T) d\epsilon - N, N = N_1 + N_2$. The scattering rate follows Fermi liquid behavior with impurities at low temperatures: $1/\tau \propto T^2 + \gamma_0$. Thus, the resistivity is expressed as $\rho \propto \frac{1}{\tau(n+p)}$. The fits to experimental data are plotted as red line in Fig. 1(b). The corresponding $n + p$ and $1/\tau$ are shown in Fig. 4. The quality of the fit suggests the insulating behavior between T^* and T_C arises from the depletion of free carriers by the opening of the pseudogap, and that the insulating to metallic resistivity crossover at T^* is a crossover temperature that originates from the competition between carrier scattering rate and population rather than from a separate electronic transition.

C. Relaxation component emerging below T_C

We now turn to the relaxation process A_2 and τ_{d2} that emerges below T_C. In a diverse assortment of other systems with small gaps near E_F, the timescale of the return to equilibrium is determined by the meV-scale kinetics of electron-hole (e-h) recombination. These kinetics may be described with the phenomenological Rothwarf-Taylor (RT) model [31]. In the RT model, the photoinduced energy populates between QPs and high-energy phonons (HEPs) through e-h recombination and excitation by HEPs. The energy dissipation is determined by the escape of HEPs. If the HEP escape rate is slow, the system will exhibit a phonon bottleneck behavior [32–35]. The observation of the significant slow rise time τ_r (Fig. 5), below T_C, as in $Ca_3Ru_2O_7$, strongly indicates that the system is in the strong phonon bottleneck regime [34], which is typically explained by an increase in scattering between hot electrons and phonons in the presence of a gap in the electronic DOS at E_F. This results in an initial excess population of HEPs compared to the quasiequilibrium condition of the bottleneck, which can excite more electrons across the gap [15].

In the small photoexcitation limit [34], the RT model relates the density of thermally activated QPs n_T to the measured transient reflectivity amplitudes A, and relaxation rates τ^{-1} as [16,34,36]

$$n_T(T) \propto \frac{A(T \rightarrow 0)}{A(T)} - 1, \tag{5}$$

$$\tau^{-1}(T) = \Gamma[\delta + 2n_T(T)][\Delta(T) + \alpha\Delta(T)T^4], \tag{6}$$

where Γ, δ, and α are T-independent fitting parameters, $\Delta(T) + \alpha\Delta(T)T^4$ describes the dependence of the high-energy phonon (HEP) decay rate on the gap size Δ, with an upper limit of $\alpha < 52/(\theta_D^3 T_{\min})$ [36], where $T_{\min} = 10$ K is the minimum temperature of the experiment. For our analysis, we assume a standard form of the thermal QP density $n_T(T) \propto \sqrt{\Delta(T)T}\exp(-\Delta(T)/T)$ [13,36,37] and a BCS-type gap of the form $\Delta(T) = \Delta_0 \tanh 2.2\sqrt{\frac{T_C}{T} - 1}$.

The amplitude A_2, and thus the thermal QP density implied by Eq. (5), can be fitted as shown in Fig. 6(a), yielding a gap size of $\Delta_0 = 7.1 \pm 0.2$ meV $= 1.71 \pm 0.05 k_B T_C$, which is close to the BCS value of 1.76. Additionally, the abrupt onset of slow rise dynamics, shown in Fig. 5, is most easily explained in the strong bottleneck regime of the RT model. Thus, we conclude that the relaxation process arises from a phonon bottleneck due to the presence of a gap in the DOS near E_F. Note that the 7.1 ± 0.2 meV gap size is in excellent agreement with 8-meV band-edge shift revealed by ARPES [10]. However, it is smaller than the 13 meV reported by optical spectroscopy measurement [4], suggesting this is an indirect gap. Using the above-extracted gap size $\Delta(T)$, the relaxation time τ_{d2} is fitted by Eq. (6) as shown in Fig. 6(b). The quality of the fits confirms the presence of a BCS-type indirect gap below T_C and the associated phonon bottleneck picture.

D. Slow relaxation component

The slow relaxation dynamics A_3 and τ_{d3} (see Supplemental Material, Sec. I [28]) are analyzed as follows. After e-ph thermalization and the escape of HEP during the phonon bottleneck process, electron and lattice subsystems reach a quasiequilibrium state with a temperature higher than environment. This pump-induced heat is then dissipated away from the probe volume through thermal conduction, which has a characteristic timescale of >500 ps. Assuming that the heat transport only occurs perpendicular to the

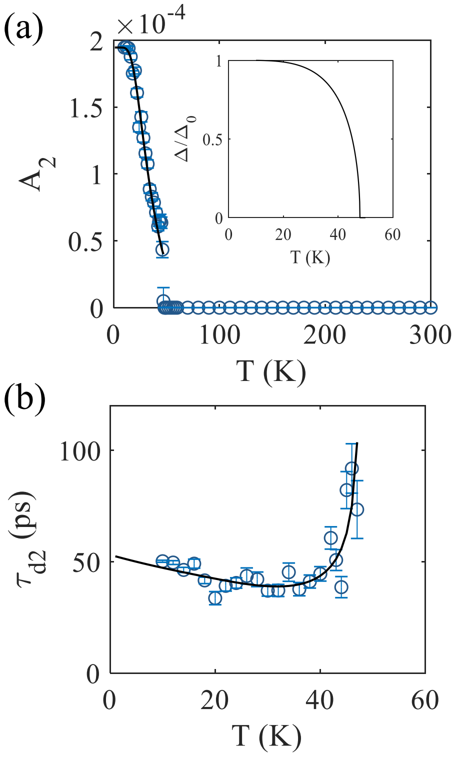

FIG. 6. (a) A finite amplitude for A_2 emerges below $T_C = 48$ K. The RT fit yields a BCS-type gap with gap size of 7.1 ± 0.2 meV at 0 K. The inset shows the T dependence of the gap size Δ/Δ_0. (b) Time constant τ_{d2} of QP relaxation dynamics. The RT fit reveals a consistent gap size of $\Delta_0 = 7.1 \pm 0.2$ meV and $\alpha = 2.39 \times 10^{-8} < \frac{52}{\theta_D^3 T_{\min}} = 6.23 \times 10^{-8}$.

sample surface, and that the sample instantly establishes an exponential temperature profile upon optical pumping with characteristic length same as the optical penetration depth, a one-dimensional (1D) solution to the surface temperature evolution can be written as

$$\Delta T = \frac{(1-R)4\pi k I_0}{\lambda C_v} e^{-\frac{16\pi^2 k^2 \sigma}{\lambda^2 C_v} t} e^{-\frac{4\pi k z}{\lambda}}\Big|_{z=0}. \qquad (7)$$

In this equation R, $k = 0.79$, $I_0 = 2\ \mu\text{J/cm}^2$, $\lambda = 800$ nm, C_v, and σ are the reflectivity, dielectric extinction coefficient (see Supplemental Material, Sec. II [28]), pump fluence, pump wavelength, total specific heat, and thermal conductivity, respectively. The change in reflection can be calculated as $\Delta R = R|_{T_0}^{T_0+\Delta T(t=0ps)}$. The experimentally measured (blue dots) and smoothed (black line) T-dependent reflectivity R are shown in the inset of Fig. 7(a). With the above equations and A_3, the 1D thermal transport model gives total specific heat C_v of $Ca_3Ru_2O_7$ as shown by open circles in Fig. 7(a). The C_v extracted by the 1D model qualitatively agrees well with calorimetry data [30] in both the magnitude and T dependence, confirming that the slow dynamics arises from thermal dissipation. The overall temperature change due to optical heating is determined to be smaller than 1 K above 30 K and increases to ~7 K at 10 K, as shown in the inset of Fig. 7(b).

Similarly, from the time-dependent behavior of Eq. (7), C_v, and relaxation time, τ_{d3}, the thermal conductivity of $Ca_3Ru_2O_7$ can be calculated as $\sigma = \frac{\lambda^2 C_v}{16\pi^2 k^2 \tau_{d3}}$. This quantity is plotted in Fig. 7(b) using open circles. To compare with these results, time-domain thermoreflectance (TDTR) measurements were carried out on aluminum-coated $Ca_3Ru_2O_7$ as a function of temperature, as shown in the Supplemental Material, Sec. IV [28]. The thermal conductivity measured on $Ca_3Ru_2O_7$ by the TDTR method is about 1.5 W/m K with very weak T dependence between 10 and 80 K [black line in Fig. 7(b)], which is of a similar order of magnitude as the values given by the 1D model. Note that this 1D model ignores the in-plane thermal transport and the possible anisotropy in thermal conductivity, hence, a perfect match to TDTR results is not expected.

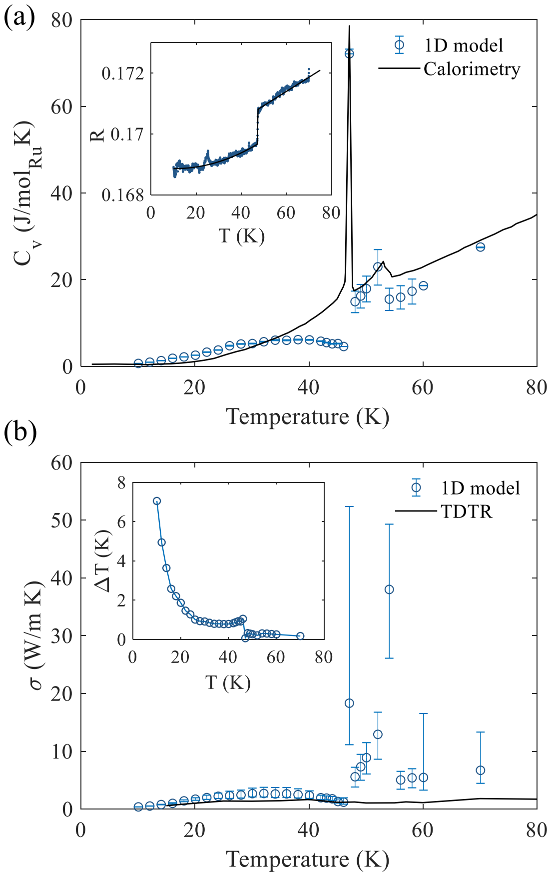

FIG. 7. (a) Heat capacity calculated by modeling the amplitude of the slow dynamics A_3 with the one-dimensional (1D) heat transport model described in the text. The black line is obtained by calorimetry measurement from literature [30]. The inset is the temperature-dependent reflectivity of $Ca_3Ru_2O_7$ at 800 nm used for the calculation. (b) The thermal conductivity extracted by using the time constant of the slow dynamics τ_{d3} under 1D model (open circles) agrees qualitatively with TDTR results (black line). The inset is the maximum temperature change induced by optical pump after electron-phonon thermalization given by 1D model.

IV. CONCLUSION

With the above analysis, we construct a comprehensive picture of photoexcited QPs relaxation dynamics in $Ca_3Ru_2O_7$ as schematically shown in Fig. 8. Below T_C, optical excitation at

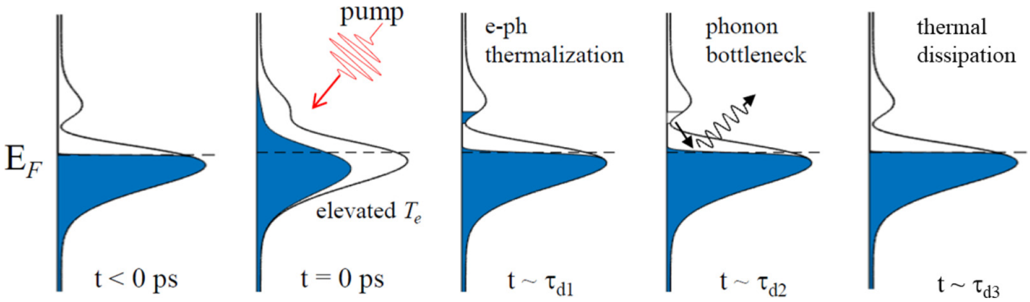

FIG. 8. Schematic of photoexcited QPs relaxation dynamics at different stages.

$t = 0$ ps increases the electronic temperature T_e, leading to a wider range of occupancy near E_F, resulting in a transient suppression of the pseudogap. The subsequent e-ph thermalization decreases the electronic temperature together with a rapid recovery of the gap on a timescale of $\sim\tau_{d1}$. However, the electrons above the gap relax on a different timescale $\sim\tau_{d2}$ limited by the kinetics of the phonon bottleneck. After the relaxation of these electrons back to the Fermi level, the electron and lattice subsystems reach quasiequilibrium with a temperature slightly higher than environment. The final slow recovery ($\sim\tau_{d3}$) is governed by the heat dissipation into the bulk of the sample, after which the system returns to equilibrium.

In summary, we present the first ultrafast optical spectroscopic study of the pseudogap phase of $Ca_3Ru_2O_7$. The T-dependent DOS yielded from the fast e-ph thermalization near Fermi surface together with the phonon bottleneck emerging below T_C provide a synergistic picture of the indirect gap. From this picture, we are able to explain the insulating to metallic crossover in resistivity at T^* as a natural consequence of the T-dependent emergence of the gap, without invoking a separate electronic transition. Given the simplicity of the TTM analysis described above, the consistency between the results yielded by the TTM on the fast dynamics and RT model on the dynamics below T_C is surprisingly good. As demonstrated by this work, the incorporation of a T-dependent DOS into the TTM can capture the influence of a gap near E_F, providing an alternative approach to unveil the evolution of low-energy electronic structure of strongly correlated metals in the time domain.

ACKNOWLEDGMENTS

Y.Y., P.K., K.C., S.L., R.D.A., and V.G. were supported by the US Department of Energy (U. S. DOE), Office of Basic Energy Sciences (BES), under Grant No. DE-SC00012375 for the experimental work, data analysis, and the travel. D.P and J.M.R. were supported by the Army Research Office under Grant No. W911NF-15-1-0017 for the DFT studies. Y.W. and Z.M. were supported by the U. S. DOE under EPSCoR Grant No. DE-SC0012432 with additional support from the Louisiana Board of Regents for the crystal growth and characterization.

Y.Y. and P.K. contributed equally to this work.

[1] A. P. Mackenzie, R. K. W. Haselwimmer, A. W. Tyler, G. G. Lonzarich, Y. Mori, S. Nishizaki, and Y. Maeno, Phys. Rev. Lett. **80**, 161 (1998).

[2] Y. Maeno, H. Hashimoto, K. Yoshida, S. Nishizaki, T. Fujita, J. G. Bednorz, and F. Lichtenberg, Nature (London) **372**, 532 (1994).

[3] H. L. Liu, S. Yoon, S. L. Cooper, G. Cao, and J. E. Crow, Phys. Rev. B **60**, R6980 (1999).

[4] J. S. Lee, S. J. Moon, B. J. Yang, J. Yu, U. Schade, Y. Yoshida, S.-I. Ikeda, and T. W. Noh, Phys. Rev. Lett. **98**, 097403 (2007).

[5] G. Cao, S. McCall, J. E. Crow, and R. P. Guertin, Phys. Rev. Lett. **78**, 1751 (1997).

[6] J. Peng, X. Ke, G. Wang, J. E. Ortmann, D. Fobes, T. Hong, W. Tian, X. Wu, and Z. Q. Mao, Phys. Rev. B **87**, 085125 (2013).

[7] Y. Yoshida, I. Nagai, S.-I. Ikeda, N. Shirakawa, M. Kosaka, and N. Môri, Phys. Rev. B **69**, 220411(R) (2004).

[8] S. Lei, M. Gu, D. Puggioni, G. Stone, J. Peng, J. Ge, Y. Wang, B. Wang, Y. Yuan, K. Wang *et al.*, Nano Lett. **18**, 3088 (2018).

[9] G. Cao, X. N. Lin, L. Balicas, S. Chikara, J. E. Crow, and P. Schlottmann, New J. Phys. **6**, 159 (2004).

[10] F. Baumberger, N. J. C. Ingle, N. Kikugawa, M. A. Hossain, W. Meevasana, R. S. Perry, K. M. Shen, D. H. Lu, A. Damascelli, A. Rost *et al.*, Phys. Rev. Lett. **96**, 107601 (2006).

[11] N. Kikugawa, A. Winfried Rost, C. William Hicks, A. John Schofield, and A. Peter Mackenzie, J. Phys. Soc. Jpn. **79**, 024704 (2010).

[12] H. Xing, L. Wen, C. Shen, J. He, X. Cai, J. Peng, S. Wang, M. Tian, Z.-A. Xu, W. Ku, Z. Mao, and Y. Liu, Phys. Rev. B **97**, 041113(R) (2018).

[13] V. V. Kabanov, J. Demsar, B. Podobnik, and D. Mihailovic, Phys. Rev. B **59**, 1497 (1999).

[14] J. Demsar, K. Biljaković, and D. Mihailovic, Phys. Rev. Lett. **83**, 800 (1999).

[15] J. Demsar, R. D. Averitt, A. J. Taylor, V. V. Kabanov, W. N. Kang, H. J. Kim, E. M. Choi, and S. I. Lee, Phys. Rev. Lett. **91**, 267002 (2003).

[16] J. Demsar, J. L. Sarrao, and A. J. Taylor, J. Phys.: Condens. Matter **18**, R281 (2006).

[17] T. Ghosh, S. Aharon, L. Etgar, and S. Ruhman, J. Am. Chem. Soc. **139**, 18262 (2017).

[18] M. Park, A. J. Neukirch, S. E. Reyes-Lillo, M. Lai, S. R. Ellis, D. Dietze, J. B. Neaton, P. Yang, S. Tretiak, and R. A. Mathies, Nat. Commun. **9**, 2525 (2018).

[19] G. Batignani, G. Fumero, A. R. Srimath Kandada, G. Cerullo, M. Gandini, C. Ferrante, A. Petrozza, and T. Scopigno, Nat. Commun. **9**, 1971 (2018).

[20] A. J. Schmidt, X. Chen, and G. Chen, Rev. Sci. Instrum. **79**, 114902 (2008).

[21] A. J. Schmidt, Ph.D. thesis, Massachusetts Institute of Technology, 2008, http://dspace.mit.edu/handle/1721.1/44798.

[22] J. P. Perdew, A. Ruzsinszky, G. I. Csonka, O. A. Vydrov, G. E. Scuseria, L. A. Constantin, X. Zhou, and K. Burke, Phys. Rev. Lett. **100**, 136406 (2008).

[23] G. Kresse and J. Furthmüller, Phys. Rev. B **54**, 11169 (1996).

[24] G. Kresse and D. Joubert, Phys. Rev. B **59**, 1758 (1999).

[25] P. E. Blöchl, Phys. Rev. B **50**, 17953 (1994); J. Lehtomäki, I. Makkonen, M. A. Caro, A. Harju, and O. Lopez-Acevedo, J. Chem. Phys. **141**, 234102 (2014).

[26] A. H. MacDonald and M. P. A. Fisher, Phys. Rev. B **61**, 5724 (2000).

[27] J. D. Pack and H. J. Monkhorst, Phys. Rev. B **16**, 1748 (1977).

[28] See Supplemental Material at http://link.aps.org/supplemental/10.1103/PhysRevB.99.155111 for supporting datasets and discussions.

[29] R. H. M. Groeneveld, R. Sprik, and A. Lagendijk, Phys. Rev. B **51**, 11433 (1995).

[30] X. Ke, J. Peng, W. Tian, T. Hong, M. Zhu, and Z. Q. Mao, Phys. Rev. B **89**, 220407(R) (2014).

[31] A. Rothwarf and B. N. Taylor, Phys. Rev. Lett. **19**, 27 (1967).

[32] J. Demsar, R. Hudej, J. Karpinski, V. V. Kabanov, and D. Mihailovic, Phys. Rev. B **63**, 054519 (2001).

[33] N. Gedik, P. Blake, R. C. Spitzer, J. Orenstein, R. Liang, D. A. Bonn, and W. N. Hardy, Phys. Rev. B **70**, 014504 (2004).

[34] V. V. Kabanov, J. Demsar, and D. Mihailovic, Phys. Rev. Lett. **95**, 147002 (2005).

[35] D. H. Torchinsky, G. F. Chen, J. L. Luo, N. L. Wang, and N. Gedik, Phys. Rev. Lett. **105**, 027005 (2010).

[36] E. E. M. Chia, J.-X. Zhu, H. J. Lee, N. Hur, N. O. Moreno, E. D. Bauer, T. Durakiewicz, R. D. Averitt, J. L. Sarrao, and A. J. Taylor, Phys. Rev. B **74**, 140409(R) (2006).

[37] E. E. M. Chia, J.-X. Zhu, D. Talbayev, R. D. Averitt, A. J. Taylor, K.-H. Oh, I.-S. Jo, and S.-I. Lee, Phys. Rev. Lett. **99**, 147008 (2007).